

The Sunyaev-Zel'dovich Infrared Experiment: A Millimeter-wave Receiver for Cluster Cosmology

W. L. Holzapfel¹, T. M. Wilbanks², P. A. R. Ade³, S. E. Church⁴, M. L. Fischer⁵,
P. D. Mauskopf^{4,6}, D. E. Osgood⁷, A. E. Lange⁴

ABSTRACT

Measurements of the Sunyaev-Zel'dovich (S-Z) effect towards distant clusters of galaxies can be used to determine the Hubble constant and the radial component of cluster peculiar velocities. Determination of the cluster peculiar velocity requires the separation of the two components of the S-Z effect, which are due to the thermal and bulk velocities of the intracluster plasma. The two components can be separated practically only at millimeter (mm) wavelengths. Measurements of the S-Z effect at mm wavelengths are subject to minimal astrophysical confusion and, therefore, provide an important test of results obtained at longer wavelengths. We describe the instrument used to make the first significant detections of the S-Z effect at millimeter wavelengths. This instrument employs new filter, detector, and readout technologies to produce sensitive measurements of differential sky brightness stable on long time scales. These advances allow drift scan observations which achieve high sensitivity while minimizing common sources of systematic error.

Subject headings: cosmology: cosmic microwave background – instrumentation: millimeter

¹Enrico Fermi Institute, University of Chicago, Chicago IL 60637.

²Aradigm Corporation, 26219 Eden Landing Road, Hayward CA 94545.

³Department of Physics, Queen Mary and Westfield College, Mile End Road, London, E1 4NS, U.K.

⁴Department of Physics, Math, and Astronomy, California Institute of Technology, MS 59-33, Pasadena CA 91125.

⁵Energy & Environment Division, Lawrence Berkeley Laboratory, 1 Cyclotron Road, MS 90-3058, Berkeley CA 94720.

⁶Department of Physics, University of California, Berkeley, CA 94720.

⁷Department of Agriculture and Resource Economics, University of California, Berkeley CA 94720.

1. Introduction

The Cosmic Microwave Background (CMB) provides a uniform back-light to the entire observable universe. Interactions between the CMB and intervening matter provide a potentially powerful probe of that matter. The hot intracluster (IC) medium gravitationally bound to rich clusters of galaxies was first discovered through its X-ray *bremstrahlung* emission. In 1972, Sunyaev and Zel'dovich (1972) argued that Compton scattering by this diffuse plasma should produce a measurable distortion of the spectrum of the CMB viewed through the cluster. This has come to be known as the Sunyaev-Zel'dovich (S-Z) effect.

The combination of the S-Z effect and X-ray emission provides an extremely powerful probe of the IC medium. Measurements of the S-Z surface brightness can be combined with the X-ray surface brightness and spectra to determine the Hubble expansion parameter (Cavaliere *et al.* 1979; Birkinshaw *et al.* 1991). The combination of the S-Z and X-ray spectra can be used to determine the radial component of the cluster peculiar velocity (Rephaeli and Lahav 1991; Holzappel *et al.* 1997b).

Due to its low surface brightness, observation of the S-Z effect is difficult, for reasons which vary with measurement frequency, angular scale, and observing platform. After many years of discrepant results, reliable detections are being made at cm wavelengths using single dish radio telescopes (Myers *et al.* 1995; Herbig *et al.* 1995; Birkinshaw *et al.* 1991), and close-packed radio interferometers (Jones *et al.* 1993; Carlstrom *et al.* 1996). Although there is strong motivation, as described below, to obtain measurements at millimeter wavelengths, these have proven even more difficult. This paper describes the instrument and method used by Wilbanks *et al.* (1994) to make the first significant detections of the S-Z effect at millimeter wavelengths.

1.1. The Sunyaev-Zel'dovich Effect

There are two velocity components of the scattering free electrons which produce the two distinct aspects of the S-Z effect. The thermal component of the S-Z effect results from the thermal motion of the electrons in the IC plasma and the kinematic component results from the bulk motion of the IC plasma relative to the CMB rest frame. The two components can be treated as independent and their brightnesses can be added linearly.

The Compton scattering, which produces the S-Z effect, preserves the number of photons, but on average increases their energy. Relative to the unperturbed CMB spectrum, the thermal component produces a decrement in brightness at low frequency and an increment in brightness at high frequency. In the nonrelativistic limit, the CMB intensity change due to the thermal component of the S-Z effect is given by (Zel'dovich and Sunyaev 1968)

$$\Delta I_{nr} = I_0 y g(x), \quad (1)$$

where $x = h\nu/kT_0$, where T_0 is the CMB temperature, and

$$I_0 \equiv \frac{2(kT_0)^3}{(hc)^2}. \quad (2)$$

The spectrum of the thermal S-Z is given by the function

$$g(x) = \frac{x^4 e^x}{(e^x - 1)^2} \left[\frac{x(e^x + 1)}{e^x - 1} - 4 \right], \quad (3)$$

which vanishes at $x_0 = 3.83$ ($\nu_0 = 217$ GHz) for $T_0 = 2.726$ K. The amplitude of the effect is given by the Comptonization parameter,

$$y = \int \left(\frac{kT_e}{mc^2} \right) n_e \sigma_T dl, \quad (4)$$

where n_e and T_e are the electron density and temperature, σ_T is the Thomson cross section, and the integral is over a line of sight through the cluster. The change in intensity due to the thermal S-Z effect is plotted in Fig. 1 for $y = 10^{-4}$, a typical value for a rich cluster. Relativistic corrections to eq. 3 are significant for typical values of electron temperature (Rephaeli 1995a) and must be taken into account in order to accurately determine the Hubble Constant and cluster peculiar velocities.

The kinematic component of the S-Z effect is due to the bulk motion of the IC plasma relative to the CMB rest frame. The scattered photons experience a Doppler shift dependent on the angle of their scattering relative to the bulk velocity. The change in CMB brightness is given by

$$\Delta I_K = I_0 h(x) \int \frac{\vec{v}_p \cdot \hat{r}}{c} n_e \sigma_T dl, \quad (5)$$

where $v_r = \vec{v}_p \cdot \hat{r}$ is the component of the bulk velocity along the line of sight toward the observer. The spectrum is described by $h(x) = x^4 e^x / (e^x - 1)^2$, equivalent to that for a change in the CMB temperature. The

change in the CMB intensity due to the kinematic component of the S-Z effect is plotted in Fig. 1 for $\tau = 10^{-2}$ and $v_r = \pm 10^3 \text{ kms}^{-1}$.

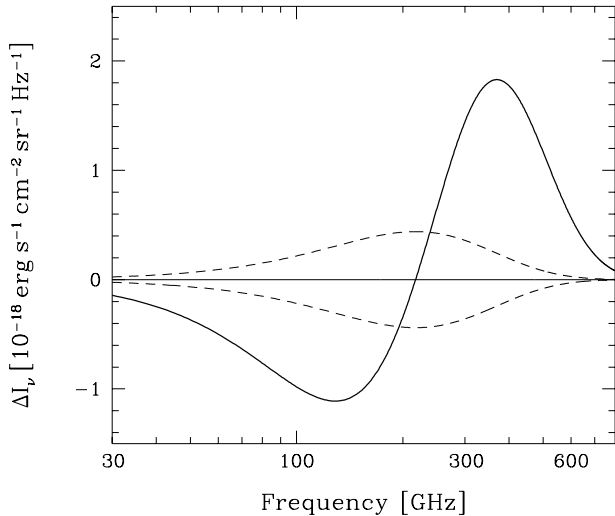


Fig. 1.— The spectra of the two components of the S-Z effect. The solid line shows the change in brightness, compared to the unperturbed CMB, of a $y = 10^{-4}$ thermal component plotted as a function of frequency. The dashed lines show the same for the kinematic component corresponding to $\tau = .01$ and $v_r = \pm 1000 \text{ kms}^{-1}$ (positive and negative curves, respectively).

1.2. Measurements at Millimeter Wavelengths

The distinct spectra of the two components of the S-Z effect allow their separation at millimeter wavelengths. In Fig. 2 we show the expected astrophysical confusion from galactic and extra-galactic sources; there is a distinct minimum at millimeter wavelengths. On arcminute scales, which correspond to the size of distant clusters of galaxies, known sources of astrophysical foreground confusion will limit the precision of millimeter-wave measurements of y and v_r to $\sim 10^{-6}$ and $\sim 100 \text{ kms}^{-1}$, respectively.

Primary anisotropies of the CMB also contribute to the uncertainty of S-Z effect measurements. The spectrum of these distortions is identical to that of the kinematic component of the S-Z effect and, therefore, they limit the accuracy with which cluster peculiar velocities can be determined. The predicted amplitude of these anisotropies is a strong function of angular

scale and cosmological model. The confusion in peculiar velocity for a cluster of optical depth τ , due to primary anisotropies of amplitude $\Delta T/T$, is

$$\Delta v_r = 100 \left(\frac{10^{-2}}{\tau} \right) \left(\frac{\Delta T/T}{3 \times 10^{-6}} \right) \text{ kms}^{-1}. \quad (6)$$

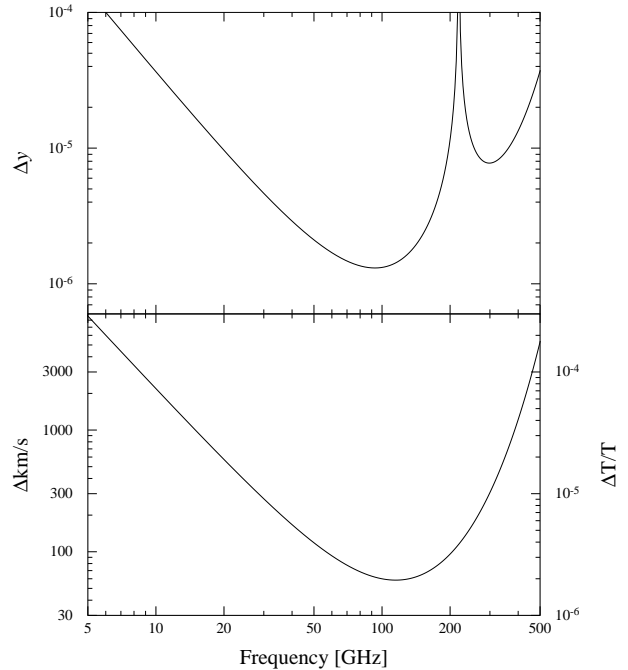


Fig. 2.— The 1σ confusion limits to measurements of the thermal (upper) and kinematic (lower) S-Z effect on arcminute scales (from Fischer and Lange 1993) as a function of frequency. The estimates include confusion from radio galaxies, IR cirrus, and infrared galaxies and assume that the S-Z source is well-matched to the beam.

Previous attempts to measure the S-Z effect at millimeter wavelengths (Meyer *et al.* 1983, Radford *et al.* 1986, Chase *et al.* 1987) have lacked the sensitivity and/or the freedom from systematic effects necessary to produce a reliable detection. Instrumental offsets and response to off-axis sources must be carefully controlled to allow accurate measurement of this low surface brightness effect (Chase *et al.* 1987, Uson 1987). In this paper we describe a high sensitivity bolometric receiver that uses a drift-scan observation strategy to eliminate the dominant sources of systematic error.

2. Instrument

The Sunyaev-Zel'dovich Infrared Experiment (SuZIE) is a bolometric array receiver for use on large aperture millimeter-wave telescopes. It is designed to separate and accurately measure both components of the S-Z effect in clusters of galaxies at moderate to high redshift ($z \gtrsim 0.1$). The instrument can be configured to observe in three mm-wave atmospheric windows. A novel read-out scheme produces stable difference signals between elements of the array, allowing drift-scan observations on time scales of minutes.

2.1. Optics

SuZIE has been used at the Caltech Submillimeter Observatory (CSO) for all observations thus far. The telescope's location at the summit of Mauna Kea provides excellent observing, with a zenith column density of precipitable water vapor ≤ 2 mm on $> 60\%$ of nights.

The receiver optics, shown in Fig. 3 and Fig. 4, are designed to couple the detectors to the telescope with minimal background loading and to maximize the overlap of the portion of the primary mirror viewed by each detector in the array. The loading is minimized by using as few warm elements as possible and by underfilling these elements to reduce spill-over.

The six detectors are mounted in low-loss cavities fed by a 2×3 array of parabolic concentrators. The 0.20 cm diameter exit apertures of the concentrators are small compared to the absorbers, making the bolometers the dominant source of loss in the cavities. The 1.63 cm diameter entrance apertures of the cones are nearly close packed on the tertiary focal surface. In time-reversed sense, the $f/2.5$ concentrators over-illuminate a 2 K, 2.5 cm diameter Lyot stop placed at an image of the primary mirror. The Lyot stop is the throughput limiting element in the system. It is sized so that the 10.4 m diameter primary mirror is underfilled by 50% in area.

Outside the Lyot stop, the beam is clear of the other apertures in the optical path. It leaves the cryostat through a $50 \mu\text{m}$ thick polypropylene window and is incident on a 33 cm diameter, 40° off-axis, underfilled ellipsoidal tertiary mirror. The measured emissivity of the $50 \mu\text{m}$ thick polypropylene window is 0.025% at $\nu = 300$ GHz, in good agreement with the published properties of this material (Afsar 1987). The tertiary mirror reimages the entrance apertures of the parabolic concentrators to the Cassegrain fo-

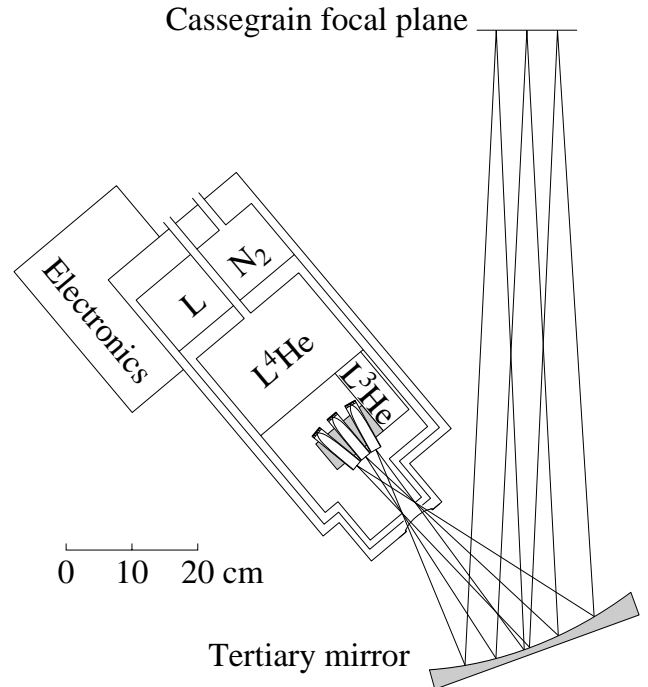


Fig. 3.— Coupling of the SuZIE receiver to the CSO using a fixed tertiary mirror. The cryostat can be rotated around its optical axis to keep the array aligned with the direction of sky drift.

cus of the CSO. The $f/\#$ of the beam emerging from the cryostat is determined by the Lyot stop, it is $f/4$ from the receiver to the tertiary and $f/10$ from the tertiary to the secondary.

The tertiary mirror is designed to simultaneously optimize the image quality across the focal plane and the overlap of the beams on the primary mirror. We have mapped the illumination of the primary mirror with a mobile 80 cm^2 chopping ambient load. The measured illumination pattern at 217 GHz falls off by -60 dB (the limit of our signal to noise) at a radius of 4.0 m. The degree of overlap of the beams on the primary determines the ability of the detector differences to subtract near field atmospheric emission. By subtracting the illumination patterns measured for the different array elements, we estimate the RMS mismatch of the beams on the primary mirror. In the row of detectors which lies closer to the optical axis, the mismatch is $\sim 4\%$ and 7% for elements separated by $2.2'$ and $4.6'$ respectively. In the row which lies further off axis after the tertiary mirror, the mismatch is $\sim 6\%$ and 10% for elements separated by $2.2'$ and

4.6' respectively. This mismatch limits our ability to remove near field differential atmospheric emission.

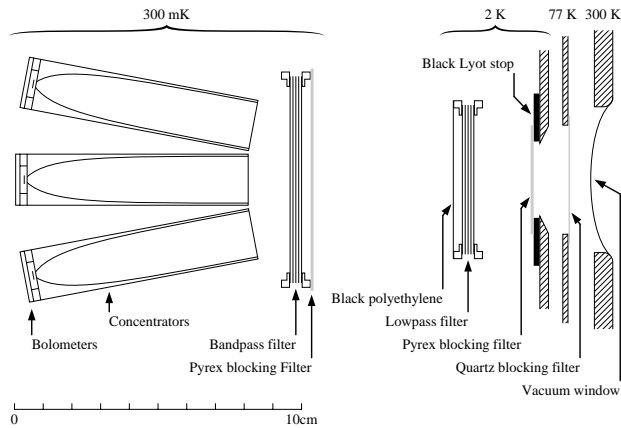


Fig. 4.— Configuration of the filters and optics inside the $L^4\text{He}$ cryostat.

2.2. Filters

The passbands are matched to atmospheric transmission windows in order to maximize the sensitivity of the system in the presence of atmospheric noise. The 142 and 268 GHz bands maximize the ratio of S-Z thermal component signal to the combination of atmosphere and detector noise. The thermal component null is near the frequency at which the kinematic component is brightest and falls within an excellent atmospheric window. By observing in this window, the 217 GHz band achieves high sensitivity to the kinematic S-Z component while minimizing the contribution of the typically much larger S-Z thermal component. The width of the band is determined by maximizing the ratio of the S-Z kinematic component signal to the sum of atmosphere and detector noise.

The passbands are defined by a combination of resonant-mesh band-pass filters and low-pass blocking filters configured as shown in Fig. 4. The blocking filters serve the additional function of minimizing the radiative heat load on the cryogenic systems from the warm optics.

A disk of fused quartz mounted on the LN_2 cooled shield absorbs radiation at frequencies between 4800 and 6×10^4 GHz, blocking most of the power from ambient-temperature sources. The thickness of the quartz is chosen to minimize the in-band reflection losses. A 0.54 mm thickness is used for observations at 142 and 268 GHz and a 0.345 mm thick disk is used

for observations at 217 GHz.

A Pyrex (Owens-Corning) glass disk mounted on the 2 K shield directly behind the Lyot stop absorbs between 900 and 6×10^4 GHz, blocking most of the power emitted by the ~ 77 K LN_2 cooled portions of the cryostat (including emission from the quartz filter) and most of the residual power from the atmosphere and other sources outside the cryostat. A 1.05 mm thickness is used for observations at 142 and 268 GHz, and a 0.67 mm thick disk is used for 217 GHz observations.

A $150 \mu\text{m}$ thick layer of polyethylene impregnated with carbon-black, LiF, and diamond dust is mounted on the 2 K stage, immediately behind a low-pass multi-element resonant mesh filter. The black polyethylene has transmission $< 10^{-3}$ at $\nu > 9000$ GHz. Together, the quartz, Pyrex, and polyethylene filters prevent any significant thermal load from reaching any of the components cooled to 300 mK by the ^3He refrigerator.

Each spectral band is defined by the response of a resonant mesh band-pass filter and a matched resonant mesh low-pass filter which blocks leaks at frequencies higher than the pass-band. The band-pass filter is located directly in front of the concentrators, the low-pass filter is located midway between the Lyot stop and the concentrators. The low-pass filter is slightly tipped to prevent resonance between the two metal mesh filters. For the 142 GHz observations, we use a low-pass filter with a cut-off of 150 GHz. In both the 217 and 268 GHz observations, a low-pass with a cut-off of 300 GHz is used. A second piece of Pyrex glass is placed in front of the band pass filter to further damp any resonance between the filters and to provide mechanical protection for the delicate mesh filter during work on the instrument.

The total spectral response, $f(\nu)$, measured using a Fourier transform spectrometer (FTS) is shown in Fig. 5 for each of the three bands. We define the central frequency of the band, when observing a source of intensity I_ν , as

$$\nu_0 = \frac{\int I_\nu f(\nu) \nu d\nu}{\int I_\nu f(\nu) d\nu}. \quad (7)$$

The width of the band is then

$$\Delta\nu = \frac{\int I_\nu f(\nu) d\nu}{I_{\nu_0}}. \quad (8)$$

We have computed the central frequency and width for observations of several sources. Because the bands

are narrow, the changes in the effective central frequencies are small. For example, the difference in the central frequency when the bands are convolved with 300 K and 3 K blackbodies is $< 0.3\%$. In Table 1, we list the central frequency and width of all six array elements for each band, where I_ν is taken to be a constant.

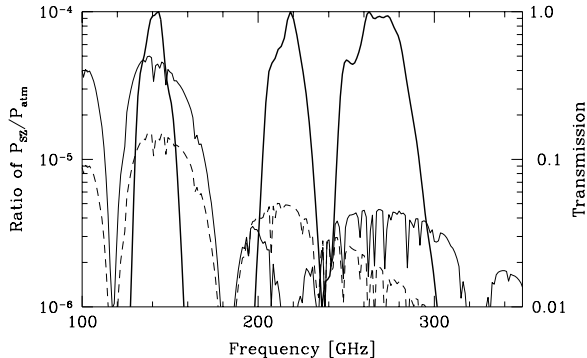


Fig. 5.— Ratio of S-Z effect power to atmospheric power, for 1 mm column density of precipitable water vapor. The fine solid line represents this ratio for the thermal component ($y = 10^{-4}$), while the dashed one represents the ratio for the kinematic component ($\tau = .01$, $v_r = 10^3 \text{ km s}^{-1}$). The heavy lines show the transmission of the complete system, measured on a Fourier transform spectrometer, for each of three frequency bands.

The beams from the elements on the outside corners of the array (1, 3, 4, and 6 in Table 1) are incident on the bandpass filter at an angle $\approx 11^\circ$ from normal, while the inside elements (2 and 5) are incident with an angle of $\approx 5^\circ$. This gives rise to systematically higher central frequencies for the outside elements of the array. The difference in central frequency between the inside and outside elements is $\sim .9\%$, $.9\%$, and $.7\%$ of the central frequency in the 142, 217 and 268 GHz bands. Although small, the differences in the spectral response of the array elements must be taken into account in order to determine accurate peculiar velocities (Holzapfel *et al.* 1997b).

In Table 2, we list the optical efficiency at the peak transmission for each of the six detector elements in the three filter pass-bands. The optical efficiencies are computed by comparing the measured difference in power absorbed by the detectors when viewing two fixed temperatures with that computed by integrating the computed difference in brightness over the mea-

sured spectral band,

$$\epsilon = \frac{(P_{T2} - P_{T1})}{A\Omega \int f(\nu) (I_{T2} - I_{T1}) d\nu}. \quad (9)$$

$f(\nu)$ is the measured filter transmission (normalized to one at its peak) and $A\Omega = .104 \text{ cm}^2 \text{ sr}$ is the maximum geometric throughput allowed by the Lyot stop. Due to the tapered illumination pattern of the parabolic concentrators, the Lyot stop is not uniformly illuminated. Therefore, the assumed throughput is an overestimate and the resultant peak optical efficiencies are lower limits to the true values. The average optical efficiencies at the peak of the bands are 37%, 42%, and 16% for the 142, 217, and 268 GHz bands, respectively. The lower optical efficiency of the 268 GHz band is due largely to the absorption of the Pyrex blocking filters.

Channel	Filter Band		
	142 GHz	217 GHz	269 GHz
1	29.2%	46.0%	13.7%
2	33.0%	36.3%	13.0%
3	37.2%	35.2%	9.3%
4	35.4%	38.5%	15.2%
5	37.9%	47.8%	15.2%
6	32.8%	49.3%	13.6%
Average	34.2%	42.2%	13.3%
σ	3.2%	6.3%	2.2%

Table 2: Optical efficiency of array elements in each of the filter bands. At the bottom of the columns we list the averages for each band and the standard deviation of the individual array elements about the mean.

Bolometers are inherently broad-band detectors; the spectral response of the instrument is defined by the filters which precede the detectors. Care must be taken to limit the response of the system to out of band radiation from sources with rising spectra. For each of the three frequency bands, we have determined the ratio of in band to out of band power when viewing the atmosphere, galactic dust, and a 300 K black-body. The model atmosphere is computed assuming a zenith optical depth, $\tau(225 \text{ GHz}) = 0.04$, and the temperature of the atmosphere to be 260 K. The dust is assumed to have a temperature of 30 K and an emissivity $\epsilon \propto \nu^{1.5}$.

The results of our tests for out of band response

Pass-band Channel	142 GHz		217 GHz		269 GHz	
	center	width	center	width	center	width
1	141.15	13.04	216.62	12.98	267.95	23.76
2	140.67	12.24	215.05	15.36	265.80	23.21
3	141.69	12.10	215.69	17.26	269.40	30.09
4	143.35	13.22	218.98	16.11	269.44	25.33
5	140.73	12.62	215.82	14.36	268.71	23.71
6	141.93	12.81	218.09	13.47	269.97	27.86
Average	141.59	12.67	216.71	14.96	268.54	25.66
σ	1.00	0.44	1.53	1.64	1.51	2.76

Table 1: Center frequency and width [GHz] of the filter bands for each detector element. At the bottom of the columns we list the averages for each band and the standard deviation of the individual array elements about the mean.

are summarized in Table 3. For the 142 and 268 GHz configurations we computed the out-of-band signal by integrating the source brightness over the spectral response of the system. The spectral response was measured from (0 – 3000 GHz), and computed at higher frequencies using transmission data obtained in our laboratory and the literature (Halpern *et al.* 1986; Bock and Lange 1995; Kudō 1972).

For the 217 GHz configuration, we did not measure the filter transmission to high frequency using the FTS. Instead, we measured the integrated system response to a quartz encapsulated mercury vapor lamp that was low-pass filtered at 1500 GHz, with and without the band blocked by a 300 GHz thick-grill high-pass filter. The limit on the ratio of out of band to in band power is $R_{MVL} = P(300 - 1500 \text{ GHz})/P_{band} < 1/500$. The computed response from frequencies > 1500 GHz is negligible in comparison. In order to determine the response of our system to sources other than the Mercury vapor lamp, we must take the different spectra of these sources into account. We treat the effective emissivity of the lamp as constant, although it actually rises with frequency due to its hot quartz envelope. For 30 K dust we assume the worst case: that all of the out of band power contribution comes from 1500 GHz. This is very conservative because the Pyrex transmission is computed to be $\sim 10^{-6}$ at this frequency. The ratio of in to out of band power from 30 K dust is then the ratio of in band to out of band power from the Mercury vapor lamp scaled by the frequency dependence of the dust emission, $R_{MVL} \times (1500/217)^{1.5}$. We can perform a similar calculation for the atmosphere by assum-

ing that the atmosphere outside the band is totally opaque. The ratio of in band to out of band power is then $R_{MVL}/(1 - e^{-\tau_{217}})$ where τ_{217} is the opacity of the atmosphere in the 217 GHz band.

By measuring the system response as a function of zenith angle, we have separated the contributions to the total optical loading from the telescope and atmosphere. The results are calibrated in terms of brightness temperature from observations of 77 and 300 K loads. In Table 4 we list the telescope and atmosphere brightness temperatures for each array element and frequency band. We have computed the brightness temperature of the atmosphere using a model incorporating FTS measurements of the atmosphere at the CSO (Lis *et al.* 1996). The model atmosphere is assumed to be ~ 260 K and the amount of precipitable water vapor is adjusted to match the measured zenith opacity, $\tau(225 \text{ GHz})$, at the time of the measurements. The results are in reasonable agreement with the model; a more detailed comparison would require information about the thermal structure of the atmosphere. The brightness temperature of the telescope was found to be ~ 30 K for all three spectral bands. This number is consistent with the results of other instruments used at the CSO; we attribute the bulk of the telescope emissivity to scattering from the secondary support structure.

2.3. Detectors

Bolometric detectors offer the highest sensitivity to continuum radiation at millimeter wavelengths. Table 5 gives a summary of the background power and background photon noise limit (BLIP) for each of the

Pass-band [GHz]	Source		
	300 K	30 K, $\epsilon \propto \nu^{1.5}$	260 K Atmosphere
142 ^a	< 0.004	< 0.024	< 0.060
217 ^b	< 0.002	< 0.036	< 0.057
269 ^a	< 0.013	< 0.035	< 0.062

Table 3: Ratio of Out-of-band to in-band response for thermal sources

^aValues determined by combining measured pass-band spectral response and calculated dielectric filter blocking (see text).

^bValues determined by combining measured out-of-band response and calculated dielectric filter blocking (see text).

3 SuZIE passbands. Sensitivity at or near the background limit can be achieved using composite bolometers cooled to 300 mK (Alsop *et al.* 1992).

Each of the SuZIE bolometers (Fig. 6) consists of a thermistor mounted on a $4 \text{ mm}^2 \times 25 \mu\text{m}$ sapphire (crystalline Al_2O_3) absorber. A coating of bismuth approximately 1000 \AA thick is evaporated on one side of the absorber. The thickness of the bismuth is chosen to maximize the broad-band absorption of light incident on the bolometer from the sapphire side. Nylon threads suspend the absorber adjacent to the exit aperture of the concentrator cone, with the bare side towards the cone.

The thermistor is constructed from a $(200 \mu\text{m})^2 \times 250 \mu\text{m}$ chip of nuclear transmutation doped (NTD) Ge:Ga (Haller 1985). The resistance of the thermistor as a function of temperature can be expressed as

$$R(T) = R_0 \exp \sqrt{\frac{\Delta}{T}}, \quad (10)$$

where R_0 and Δ are properties of the thermistor and T is its temperature. Δ is determined by the doping of the NTD, which is extremely uniform for the single batch from which all the thermistors are constructed. R_0 is determined by the geometry of the thermistor but is also effected by mechanical stress. In order to mechanically support and provide electrical and thermal contact to the thermistor without stressing it, gold wires $20 \mu\text{m}$ in diameter are wedge-bonded to the gold contacts of the thermistor. These wires are attached to the bare side of the absorber with epoxy. The large heat capacity of the gold leads dominate the heat capacity of the bolometers. The measured thermal time constants of $\tau \sim 50 - 100 \text{ ms}$ easily satisfy the modest requirements of our drift scanning (slow modulation) observations.

Superconducting niobium-titanium (NbTi) wires

connect the gold wires to thermally sunk electrical contacts on the bolometer mounting ring. These $12 \mu\text{m}$ diameter leads are copper clad at the ends, where they are indium soldered to the gold leads and lead-tin soldered to the mounting ring electrical contacts. The portions of the NbTi wires with no copper cladding are $\approx 4 \text{ mm}$ long; together the two leads contribute a thermal conductivity, $G \approx 10^{-10} \text{ WK}^{-1}$. The bolometer is connected to the rest of the electrical circuit by $125 \mu\text{m}$ Manganin wires.

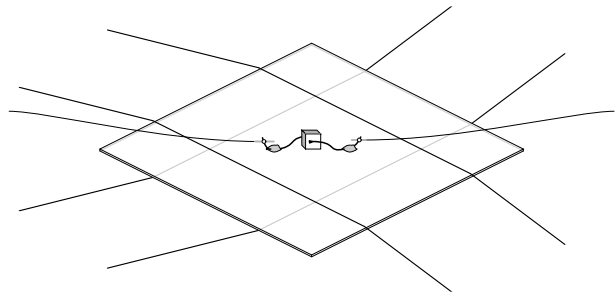


Fig. 6.— A composite bolometer used in the SuZIE instrument. The thermistor with wedge-bonded gold leads is secured to the sapphire substrate with two blobs of epoxy. The NbTi electrical leads have copper-clad ends, which are soldered to the gold wires. The substrate is suspended by four nylon threads.

Fine nylon threads $\sim 15 \mu\text{m}$ in diameter (12 denier 8 filament Nylon type 782 bright, E. I. Du Pont de Nemours and Company) support the absorber and provide a thermal conductivity of $G \approx 10^{-9} \text{ WK}^{-1}$ at the operating temperature of the bolometers. For optimal performance, each spectral band could have a set of detectors with the support structure optimized for the measured system loading. Instead, we compromise and choose the thermal conductivity so that

Pass-band [GHz]	$\tau(225\text{ GHz})$	Telescope	Atmosphere	Model Atmosphere
		Brightness Temperature [K]		
142	.045	29.6 ± 4.0	6.5 ± 1.3	5.51 ± 0.04
217	.048	26.1 ± 2.2	8.4 ± 0.5	11.68 ± 0.14
269	.031	28.4 ± 1.0	10.8 ± 0.3	14.06 ± 0.57

Table 4: Telescope and Atmospheric temperature computed from sky dips. The uncertainty in the measured telescope and atmosphere temperatures are the standard deviations of the results for each array element about their mean. The uncertainty in the model atmosphere temperature is the standard deviation of the calculated power in the six array elements from the integrals of the model atmosphere (computed for $\tau(225\text{ GHz})$) over the measured spectral bands.

Pass-band [GHz]	P_{scope}	P_{atm}	P_e	BLIP	Detector	Measure d
		[pW]		NEP [$10^{-17}\text{ W Hz}^{-1/2}$]		
142	10.8	2.2	75.0	4.9	14.7	29.8
217	26.3	6.7	87.7	9.7	16.7	72.1
269	22.2	7.7	123.0	10.4	18.0	125.2

Table 5: Background power and sensitivity. P_e is bias power dissipated in the thermistor, P_{scope} is emission from warm telescope, and P_{atm} is atmospheric emission. BLIP is the noise contribution to a single detector due to the statistical arrival of background photons. Detector NEP includes contributions due to Johnson, phonon and amplifier noise and is listed is for a single detector. Measured NEP is from telescope scans and includes the contribution of the atmosphere (measured at 125 mHz).

the same set of detectors can be used under the range of background powers encountered in all three spectral bands. The measured detector noise equivalent power is $NEP \approx 1.2 \times 10^{-16}\text{ W Hz}^{-1/2}$ at optimum bias (in the dark). This noise level is comparable to the background photon noise in the 217 and 268 GHz bands (Table 5).

The detectors must be well matched to provide acceptable performance in the bridge readout (Section 2.4). In order to provide a large common mode rejection ratio (CMRR) to atmospheric noise, the thermal conductivity of the detectors should be matched to better than 5%, while the parameters describing the thermistor resistance, R_0 and Δ , should be matched to better than 5% and 1%, respectively (Glezer *et al.* 1992). Matching of thermistor characteristics is ensured by the uniform doping of the NTD Ge:Ga material and careful control of the geometry and contacting of the thermistors. The matching of the detector thermal conductivities is controlled by the use of uniform materials and strictly defined geometries for the substrate and mounting. The values of R_0 , Δ , and G for the six bolometers are given in Table 6. The measured dispersion of the values of R_0 ,

Δ , and G about their mean are 4.8%, 0.8%, and 5.2%, respectively. When biased identically, the detectors within a given row have output voltages matched to a within $\approx 1\%$ (Fig. 7). During observations, when the bias currents are adjusted to match the responsivities of the detectors to common mode atmospheric emission, the output voltages of the detectors match within $\approx 1.5\%$. To improve the detector matching and maintain a high CMRR in the presence of changing background power, the detectors are usually biased with a large current, 10 – 15 nA, this decreases the sensitivity to $NEP \approx 1.5 - 2.0 \times 10^{-16}\text{ W Hz}^{-1/2}$. As is shown in Table 5, the system noise is dominated by atmospheric noise; a small decrease in detector sensitivity has little effect on the performance of the instrument.

2.4. AC Bridge

The major technical advance represented in this instrument lies in the low-frequency stability of the bolometer difference signals. This low-frequency stability, provided by a balanced AC bridge readout, allows drift-scan observations to be made with no mechanical modulation of the beam and with the tele-

Channel	$R_0(\Omega)$	Δ	$G(pW/K)$
1	13.9	51.2	1015
2	14.6	51.6	955
3	14.3	51.0	1055
4	15.4	50.7	946
5	15.6	51.6	878
6	14.0	51.3	976
Average	14.6	51.2	963
σ	0.7	0.4	50

Table 6: Bolometer characteristics. The thermal conductivity is measured in the dark at the operational temperature of the bolometers in the 142 GHz band.

scope fixed relative to the Earth. In this observation mode, only celestial sources of emission are modulated. The ratio of time on and off source is comparable to that for a multi-level differencing scheme (Herbig *et al.* 1995).

Each AC-bridge contains a pair of matched bolometric detectors and bias resistors as shown in Figure 8 (Rieke *et al.* 1989; Wilbanks *et al.* 1990; Devlin *et al.* 1991). The bolometers register a small change in optical power as a proportional change in the resistance of the thermistor. The circuit described here produces a stable voltage proportional to the difference in resistance between two detectors. We use this circuit in the SuZIE receiver to difference between pixels in the focal plane, allowing us to determine the differential brightness of two points on the sky without modulation of the incoming beam. In principle (for perfectly matched detectors and optics), this readout system perfectly suppresses signals due to fluctuations in bias amplitude, amplifier gain, heat-sink temperature, and common mode atmospheric noise.

This system is still susceptible, as are chopping systems, to noise due to differential atmospheric emission. In this regard, the differencing is equivalent to square-wave beam-switching at infinite frequency. True differential noise arises because the six beams in the array are each sensitive to emission from slightly different columns of atmosphere. Adjusting the bias current of a detector changes its voltage responsivity to absorbed power; this allows the responsivities of the detectors to be accurately matched. Glezer *et al.* (1992) showed that, in general, it is possible to null the response of the detector differences to common-

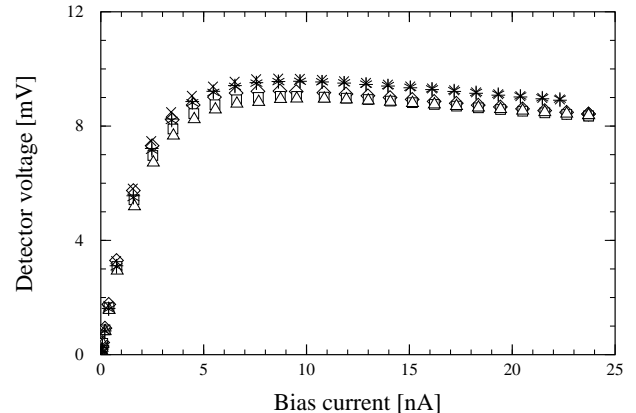


Fig. 7.— Plot of six bolometer I-V curves. The non-ohmic behavior, shown in the roll-over at ~ 5 nA, is caused by electrical self-heating in the detector. The excellent matching of the detectors is evident, especially at high bias. The six detectors cluster into two rows of three in which the voltages are virtually identical.

mode optical signals for reasonable ratios of electrical bias power to incident optical power. They also point out that the CMRR, in the presence of changing optical loading, is improved by increasing the detector bias power beyond the point where maximum signal to noise is obtained in the absence of common mode optical signals.

2.5. Read Out Electronics

The SuZIE detector electronics, shown in Fig. 9, are configured to take differences only along the long direction of the array. Among the three detectors in a row, the electronics read out all three possible differences, giving a total of six for the array.

The voltages of the detectors in each bridge are buffered by a matched pair of cold JFET (NJ132L, InterFET Corp.) source followers (six pairs total for the six differences). The JFETs are mounted on the 2 K cold-plate and connected to the 300 mK stage by short, tightly constrained Manganin leads. The proximity of this first amplification stage to the detectors isolates the high-impedance points in the circuitry from the wiring out of the cryostat, minimizing the amount of wiring susceptible to microphonic pickup, channel-to-channel crosstalk, and radio frequency interference. The JFETs are thermally isolated from the 2 K cold-plate on fine fiber-glass stalks

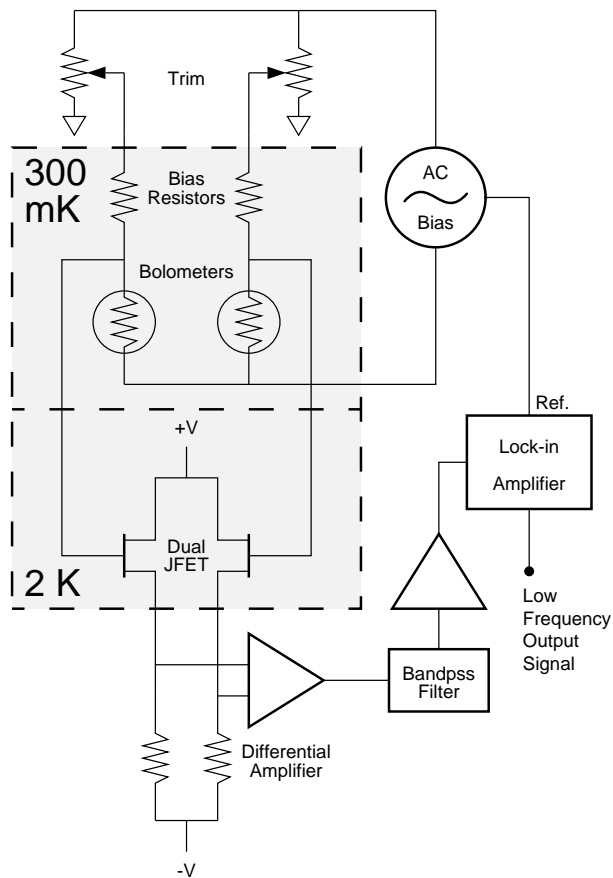


Fig. 8.— AC-bridge readout for bolometers. The bias resistors are large compared to the trim resistors, which are needed to compensate for mismatches in the bolometer responsivities. The initial amplification stage is mounted on the ^4He cold-plate to reduce the amount of high impedance wiring. In the SuZIE experiment, both bolometers are exposed to the sky, and the output is proportional to the differential sky brightness.

to allow them to maintain an operating temperature near 100 K. They are encased in 2 K copper cavities to prevent their thermal radiation from reaching other parts of the instrument. At the operating frequency of ~ 100 Hz, the JFET source followers exhibit no $1/f$ noise and each contributes $\approx 2.0 \text{ nV Hz}^{-1/2}$ noise to the signal it buffers. The bridge is biased with a square-wave bias rolled off at frequencies above the third harmonic. All three detectors in a row are driven by a common bias; the two rows operate at different frequencies, both near 100 Hz. At this fre-

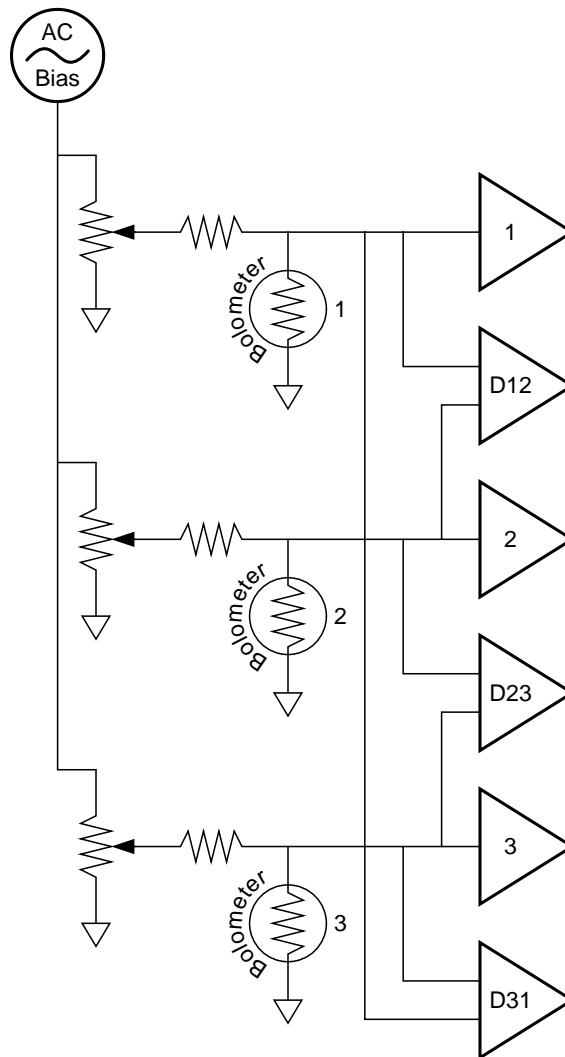


Fig. 9.— One row of the SuZIE readout electronics. Each row has a single bias, three difference channels, and three absolute channels.

quency, the amplifiers have low noise and the bias oscillations are much faster than the bolometer time constants. The buffered detector signals are subtracted in a low noise differential amplifier and the difference signal is demodulated in a square-wave lock-in amplifier. A filter, similar to that used to roll-off the bias, is placed before the input of the lock-in to reduce the sensitivity of the demodulated signal to noise near higher harmonics of the fundamental. The outputs of the demodulators pass through 2-pole low-pass Bessel filters set at 2.25 Hz, just less than half the 5 Hz A/D sampling frequency. Outside the cryo-

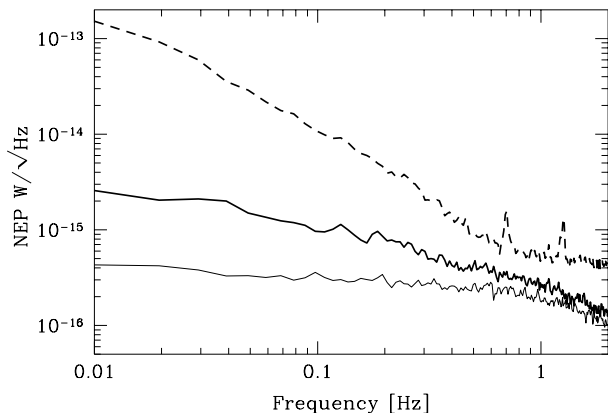


Fig. 10.— SuZIE system noise for a detector difference as measured in the laboratory with an optical blank in place of the Lyot stop (solid line). Also shown is the noise for the system at the telescope in the 217 GHz configuration, for both a single detector (dashed heavy line) and for a detector difference (heavy line). The results are calibrated in terms of NEP using the measured electrical responsivity of the detectors.

stat electronics box, another amplification stage removes DC offsets from each channel and matches the dynamic range of the signals to the analog-to-digital converter. This gain stage includes an additional set of 2-pole anti-aliasing low-pass Bessel filters set to 2.25 Hz. Six similar circuits read out the voltage on each bolometer individually. These are essential for characterizing the behavior of the instrument and the detectors. They also provide a measure of sky brightness over time. For these circuits, the signals pass through AC-coupled amplifiers before the demodulators. The gain of the single detector readouts is 500 compared with 7×10^4 for the difference channels. In Fig. 10 we show the noise, normalized to unity gain, for a single detector and the 4.3' difference viewing the sky in the 217 GHz band. The system noise in both the single detectors and differences is dominated by atmospheric emission. Between 10 and 100 mHz (the signal bandwidth for drift scans over a cluster) the CMRR to atmospheric noise ranges from ~ 60 to 10.

The 12 bolometer signals, two channels monitoring the amplitude of the bias voltages, and two channels that monitor the temperature control circuitry (see section 2.7.) are read by a 16 channel, 16-bit A/D converter (Model 576 High Speed Data Logging System, Keithley Instruments, Inc.) and transferred to

an Apple Macintosh IIfx computer using IEEE-488 communications.

2.6. Parallax Alignment Rotator

The SuZIE system is designed specifically for drift-scan observations made with the telescope immobilized. In this scheme, the telescope is pointed west of the source and fixed in altitude and azimuth. The earth's rotation then sweeps the telescope beam over the source. In order to orient the array with the rows aligned East/West so that the source drifts sequentially through each of the three pixels in a row, the entire receiver is mounted in bearings that rotate about the optical axis. At 0° rotation angle the array is parallel to the horizon, appropriate for observing sources at transit. The receiver can be rotated by angles up to 90° in either direction from this position to allow observation of sources rising to the east or setting to the west of the telescope.

A computer controlled stepper motor keeps the array aligned with the scan direction, updating the rotation angle at the beginning of every scan (≈ 2 minutes). A precision ten-turn variable resistor is engaged to the belt that turns the receiver. Its resistance is calibrated and then monitored to ensure the integrity of the mechanical linkage from the stepper motor to the receiver.

2.7. Cryogenics

The SuZIE receiver is built into a liquid helium cryostat with a liquid nitrogen cooled intermediate heat shield (Infrared Laboratories). The $L^4\text{He}$ and LN_2 tanks have 4.5 liter and 3 liter capacities, respectively. During operation, the $L^4\text{He}$ bath is pumped to achieve cold-plate temperatures below 2 K. Both the concentrators and the detectors are enclosed within the $L^4\text{He}$ cooled heat shield. They are thermally isolated from the $L^4\text{He}$ cold-plate on Vespel (E. I. Du Pont de Nemours and Company) tubes and cooled to 300 mK by a ^3He refrigerator. The ^3He refrigerator is a self-contained charcoal sorption pump refrigerator, similar to those described by Duband *et al.* (1991). The refrigerator holds 4 STP liters of ^3He gas at 6 – 7 MPa at room temperature, and has a hold-time of more than 12 hours. The operating temperature of the detector cold-stage is ~ 305 mK under the heat load in the receiver; it is raised to 314 mK in order to facilitate temperature control.

Initial temperature control using commercially

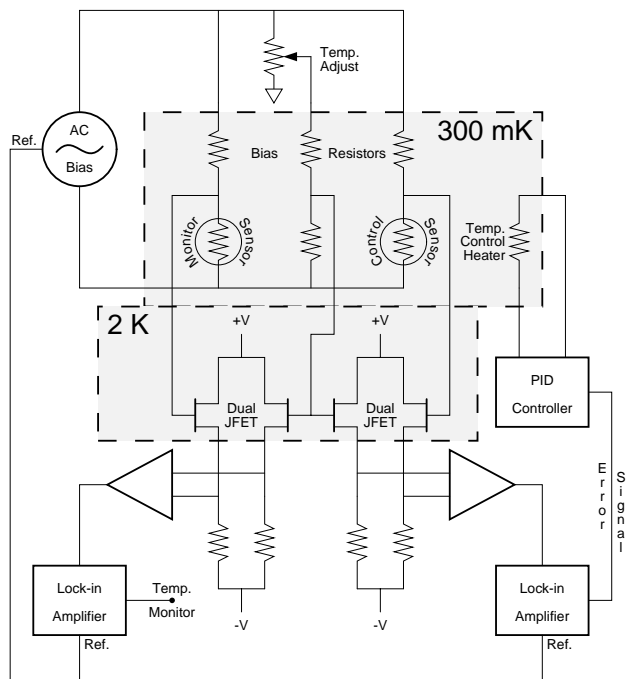


Fig. 11.— The SuZIE temperature control electronics. Two thermometers mounted on the optics block are differenced against fixed resistors. A variable bias resistor allows adjustment of the temperature set point. The output from one bridge is used as the error signal for a proportional-integral-differential (PID) controller, which closes the control loop using a heater on the optics block. The other bridge is monitored to determine the temperature stability.

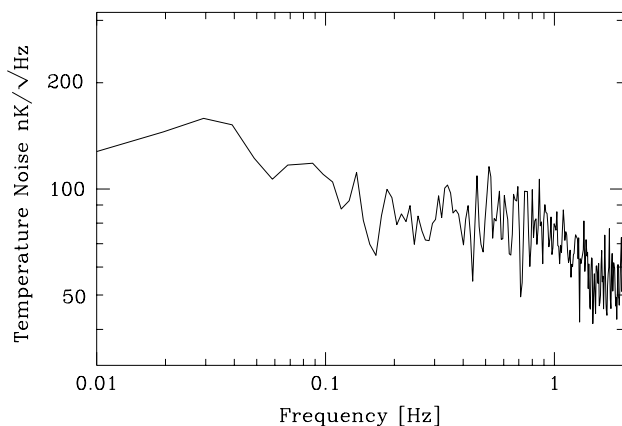


Fig. 12.— Measured temperature noise of the 300 mK cold stage monitor thermistor.

available instruments was unsatisfactory and a customized precision temperature control system was developed. Although the commercial sensor (GRT-200, Lakeshore Cryotronics) and resistance bridge thermometer readout (AVS-46 Resistance Bridge, RV-Elektronikka Oy) were retained to monitor the absolute temperature, additional sensors and readouts were installed for the control circuit (Fig. 11). Two NTD Ge:Ga thermistors are mounted, via gold electrical leads, to heat-sinks on the detector cold-stage. The two sensors operate independently, one to control the temperature and the other to monitor its value. The thermistors are read out in bridge circuits identical to the bolometer readout circuits, except the thermistors are differenced with a fixed resistor. The fixed resistor is chosen to be close to the resistance of the thermistors at the chosen operating temperature. Fine adjustment of the operating temperature is possible by changing the relative biasing of the resistor and thermistor. The output of the control sensor bridge circuit is input to a commercial PID controller (TS-530 Temperature Controller, RV-Elektronikka Oy) which feeds back to a $500\ \Omega$ heater resistor on the detector cold-stage. At the operating temperature of 314 mK, the heater supplies $5\text{--}10\ \mu\text{W}$ of power to the cold-stage. The output of both the control and monitor sensor circuits are amplified and logged as for the detector differences.

The PID controller is operated to keep the control thermistor-resistor bridge output equal to zero. The monitor circuit then provides a measurement of the difference in temperature (if any) between the two thermistors and an estimate of the temperature fluctuations in case the control thermistor malfunctions. In Figure 12, we show the Power Spectral Density (PSD) of the temperature fluctuations measured by the monitor circuit. The temperature of the 300 mK cold stage fluctuates by $< 150\ \text{nK Hz}^{-1/2}$ on time-scales of 100 s. These fluctuations make a small contribution to the total noise of a single detector, $NEP_T < 5.4 \times 10^{-17}\ \text{W K}^{-1}$. The bolometer differences exhibit measured CMRRs to temperature fluctuations ranging from 12 to 360. The contribution of the measured temperature fluctuations to the detector noise is $NEP_T < 3.4 \times 10^{-18}\ \text{W K}^{-1}$ for the most poorly matched detector pair.

In operation at the telescope, there is a small signal in the temperature monitor at the beginning of the scan due to the telescope motion heating the cold stage by $\lesssim 100\ \text{nK}$. The cold stage recovers from this

impulse with a time constant of ~ 7 s. Although not visible in a single scan, this feature is significant in the coadded temperature monitor scans. In Church *et al.* (1996) the effect of this signal on the data channels is investigated by correlating the co-added differential signals to the temperature monitor signal; no significant correlation is found.

3. Beam-shapes and Calibration

The instrument makes a differential measurement of the sky brightness between pairs of array elements. Accurate calibration requires a knowledge of the spectral response (see Sec. 2.1.), the shape of the beams on the sky, and the responsivity of the array.

The shapes of the beams are determined by drift-scan observations of planetary calibrators. A map of the single-detector beam patterns measured at 142 GHz with drift scans across Jupiter is shown in Figure 13. Scans were performed with the array offset in declination from the source (transverse to the scan direction) by steps of $15''$. The angular size of Jupiter ($\sim 40''$) broadens the measured beams slightly. The beams are separated by $2.2'$ (adjacent) and $4.3'$ (end-to-end) along the direction of the rows. The full

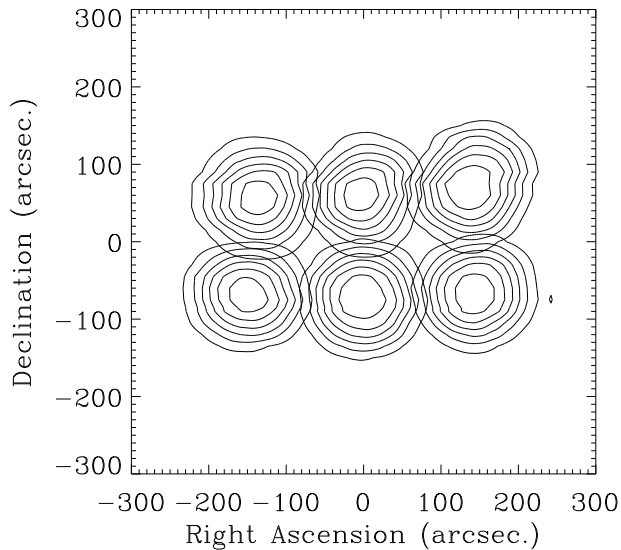


Fig. 13.— Map of bolometer single channels at 142 GHz constructed from drift scans across Jupiter spaced by $15''$ in declination. Contours correspond to 0.9, 0.75, 0.6, 0.45, 0.3 and 0.15 of maximum. The large size of Jupiter ($\sim 40''$) broadens the beams slightly.

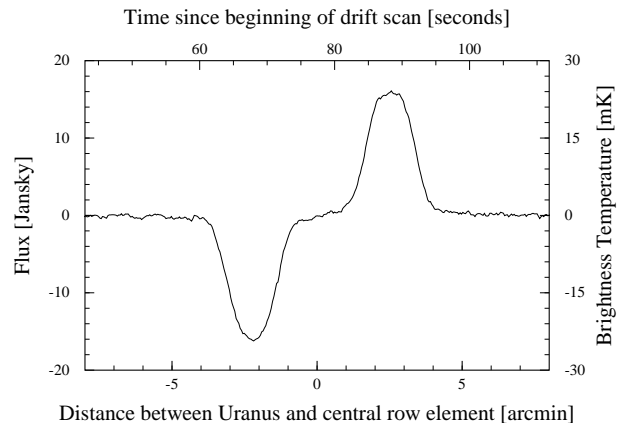


Fig. 14.— 142 GHz band response of $4.3'$ difference drift scanned across Uranus. The brightness temperature axis corresponds to a source that fills the ~ 3 arcminute² beam.

width at half maximum (FWHM) and integrated solid angle of each array element, measured for each of the three spectral bands, are listed in Table 7. The planets used in these measurements, Mars and Uranus, had angular diameters $\sim 3''$ and $\sim 2''$, small enough to be neglected in the determination of the beam parameters. The parameters listed for the 142 GHz and 217 GHz bands were measured after the installation of a new tertiary mirror, which significantly improved the measured beam patterns. The improved matching of the beams is evident from the reduced scatter when compared to the 268 GHz band beams measured in 1993 with the original tertiary mirror. After the installation of the new tertiary mirror, the measured FWHM for the pixels in the array match to within the accuracy of our measurement ($\approx .05'$).

The planet scans provide the absolute calibration of the instrument. The output signals are divided by the known source brightness, yielding the responsivity to celestial sources. The observations at 142 and 217 GHz (April 93; April and May, 1994) were calibrated by comparing scans over Uranus (Figure 14) with the brightness model of Griffin and Orton (1993) integrated over the measured spectral bands. The 268 GHz observations (May 1993) were calibrated with Mars assuming a brightness temperature of 195.6 K (Orton *et al.* 1986).

4. Scan Strategy

We have developed a scan strategy that minimizes and provides sensitive tests for systematic errors. The

Pass-band	142 GHz		217 GHz		269 GHz*	
Channel	FWHM (arcmin)	Ω (arcmin ²)	FWHM (arcmin)	Ω (arcmin ²)	FWHM (arcmin)	Ω (arcmin ²)
1	1.78	3.25	1.93	3.75	1.57	2.39
2	1.83	3.19	1.99	4.19	1.70	2.82
3	1.77	3.16	1.97	3.74	1.92	3.44
4	1.74	3.11	1.87	3.46	1.91	3.45
5	1.68	2.96	1.88	3.71	1.78	3.20
6	1.80	3.42	1.91	3.46	1.60	2.50
Average	1.77	3.18	1.92	3.72	1.75	2.97
σ	0.05	0.15	0.05	0.27	0.15	0.47

Table 7: Full Width Half Maximum (FWHM) and solid-angle (Ω) of the beams for each array element, as determined from scans of Mars and Uranus.

(*) The 269 GHz beams were measured with the original tertiary mirror.

telescope acquires a position leading the source by a right ascension offset (RAO) and tracks that position. The array is rotated such that the rows of detectors lie along lines of constant declination. To begin the scan, the tracking is disabled and the telescope maintains a fixed altitude and azimuth. The rotation of the earth then moves the beams in increasing RA at a rate of $.25 \cos(\delta)'/s$. During the scan, there are no moving parts and only celestial sources are modulated. After drifting for $\sim 30'$ the scan ends and the telescope re-acquires the position leading the source. During all observations, we alternate the RAO of sequential scans between $12'$ and $18'$.

Because of the low surface brightness of the S-Z effect, we have to combine many scans in order to produce a significant detection. Our results are, therefore, sensitive to the presence of any scan correlated instrumental baseline. We check for such a instrumental baseline in two ways.

First, we observe patches of sky free of known sources. We analyze the data in the same way as the source data. An instrumental baseline would be detected as a non-zero signal when the source model is fit to the scan data. In 1994, we accumulated 8.5 hours of data on one patch of sky centered at ($10^h 24^m 25^s$, $3^\circ 49' 9''$ J2000), and 7.5 hours on a second patch centered at ($16^h 32^m 44^s$, $5^\circ 49' 43''$ J2000). Fitting this data to an isothermal source model described by ($T_e = 10$ keV, $\beta = 2/3$, $\theta_c = 1.2'$), we find a central Comptonization $y_0 = 1.5 \pm 2.2 \times 10^{-5}$. Therefore, to this level of sensitivity, sufficient for observations of a large sample of clusters, we find no significant baseline. We have also determined the in-

strumental baseline when observing in the 1.4 and 1.1 mm bands. We find no significant baseline; however, because of the much larger sky noise, the limits are less sensitive.

Although a baseline must be correlated between several scans to be significant, it could vary on long time-scales. For this reason, it is preferable to check each source observation for the presence of an instrumental baseline. In the observations, the RAO is alternated between scans in order to make such a test possible. Alternating the RAO moves the source by $\Delta\text{RAO} = 6'$ while any baseline is unaffected. Subtracting sequential pairs of scans then removes the baseline with only a small effect on the signal. The subtracted scans are fit with the difference of two source models offset by ΔRAO . In Holzapfel *et al.* (1997a) this method is used to test for the presence of an instrumental baseline in the 142 GHz data for A2163. In all cases, there is no significant change in the results when the scans are differenced, indicating that there is no significant instrumental baseline.

5. Sensitivity

The sensitivity of the system to point sources is determined from the measured responsivity and noise. Fig. 15 shows the PSD of the noise for the same $4.3'$ difference during observations in the 142, 217, and 268 GHz configurations. The noise performance at frequencies below 300 mHz is dominated by noise resulting from differential atmospheric emission. The atmospheric noise varies considerably from one observation to another; the data shown here are chosen to

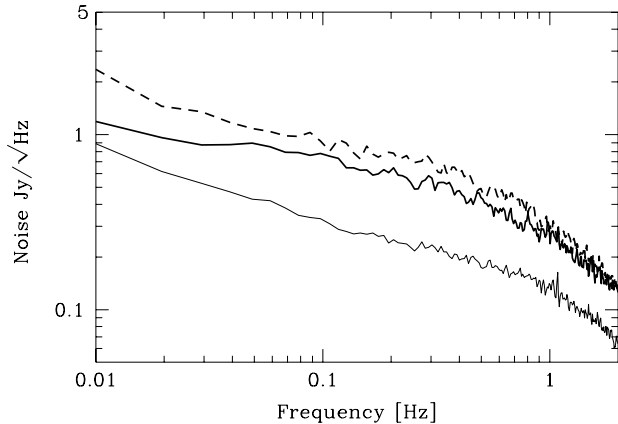


Fig. 15.— SuZIE system noise for the difference between 2 detectors separated by $4.3'$. The solid line corresponds to the 142 GHz band, the heavy line the 217 GHz band, and the dashed line the 268 GHz band. The data for three spectral bands are calibrated in terms of Janskys by observations of planets.

be representative of the performance in good weather. At frequencies of ~ 125 mHz the sensitivities in the $4.3'$ difference are approximately $300 \text{ mJy Hz}^{-1/2}$, $800 \text{ mJy Hz}^{-1/2}$, and $1000 \text{ mJy Hz}^{-1/2}$ for observations in the 142, 217, and 268 GHz bands.

We have used observations of S-Z sources to characterize the sensitivity of the system to central Comptonization and peculiar velocity. An isothermal model for the surface brightness is computed assuming the IC gas to be described by ($T_e = 10 \text{ keV}$, $\theta_c = 1.2'$, $\beta = 2/3$). Relativistic corrections have been taken into account; they decrease the sensitivity to y slightly. The source model is convolved with the measured beam patterns in order to determine a template for the bolometer difference signals during the drift scan. All six bolometer differences are fit to the source template in order to determine the source amplitude for each scan. The uncertainty is determined from the scatter of the values obtained from each scan about their weighted mean. The sensitivities achieved for the three spectral bands are listed in Table 8; these are the results of 5 – 7 hours of observation taken on each of three separate nights. The atmospheric noise is extremely variable, resulting in values of noise as much as two times larger than these values on some nights. The atmospheric noise is correlated with the zenith optical depth $\tau(225 \text{ GHz})$, however, it is more strongly correlated with the instability of $\tau(225 \text{ GHz})$

over the course of an evening.

We have also determined the sensitivity of the SuZIE system to changes in the temperature of Rayleigh-Jeans and CMB sources. We assume that one beam of a detector difference is completely filled by the perturbed temperature. The noise used in the calculation is for ~ 125 mHz which corresponds to the time spent on a $\sim 2'$ beam when drift scanning. The resultant sensitivities for the three spectral bands are listed in Table 8.

6. Applications to Cosmology

6.1. Hubble Constant

Using the SuZIE system, we have detected decrements in the brightness of the CMB in the direction of the clusters A2163, A1689, A1835, A2204 and ZW3146 with significance greater than 6σ . In Holzapfel *et al.* (1997b), we combine observations of the S-Z effect in A2163 with X-ray data in order to determine the Hubble constant. Assuming the IC gas to be isothermal, and including many possible sources of systematic error, we find $H_0 = 60^{+45}_{-31} \text{ kms}^{-1}$ at 68% confidence, where the uncertainty is dominated by the IC gas temperature. Adopting the thermal structure determined by ASCA (Markevitch *et al.* 1994), $H_0 = 78^{+60}_{-40} \text{ kms}^{-1}$.

The uncertainty in the distribution of the IC gas along the line of sight limits the accuracy of a Hubble constant determined from only one cluster to $\sim \pm 27\%$. In order to reduce this uncertainty we must average the results of a carefully selected sample of clusters while taking care to control systematic errors. The uncertainty in the ellipticity will dominate if we are able to determine y to approximately 15% accuracy. In the ROSAT all sky survey (Ebeling *et al.* 1996) there are ~ 25 clusters at redshift $z > 0.2$ with $L_X(0.1 - 2.4 \text{ keV}) > 10^{45} \text{ erg s}^{-1}$; we estimate these clusters to have $y \gtrsim 1.5 \times 10^{-4}$. In ~ 10 hours per cluster, the SuZIE instrument can make observations of the S-Z effect which, assuming high quality X-ray data, can be used to determine H_0 with uncertainty limited by cluster ellipticity.

6.2. Peculiar Velocities

Galaxy clusters have been shown to be efficient tracers of the large-scale velocity field of the universe (Bahcall *et al.* 1994; Gramann *et al.* 1995). We have used measurements at mm wavelengths to constrain

Pass-band [GHz]	Δy $10^{-5}\sqrt{\text{Hr}}$	$\Delta v_r \times (0.01/\tau)$ [kms $^{-1}\sqrt{\text{Hr}}$]	ΔT_{RJ} [mK $\sqrt{\text{s}}$]	ΔT_{CMB} [mK $\sqrt{\text{s}}$]
142 GHz	6.8	2010	1.3	2.1
217 GHz	–	3190	0.9	3.5
269 GHz	29	5500	1.1	5.7

Table 8: Typical sensitivity to y and v_r for a cluster with isothermal IC gas described by ($T_e = 10$ keV, $\theta_c = 1.2'$, and $\beta = 2/3$). Also listed are the raw sensitivities for a signal that completely fills one beam of the difference, where ΔT_{RJ} and ΔT_{CMB} correspond to changes in temperatures of Raleigh-Jeans and CMB sources.

peculiar velocities of the clusters A1689 and A2163. Unlike the determination of the Hubble constant, the details of the IC gas distribution are not important to the determination of the peculiar velocity. The resulting peculiar velocities depend weakly on the IC gas temperature. The uncertainty is dominated by the statistical uncertainty in the amplitude of the S-Z kinematic component. The combination of 142, 217, and 268 GHz measurements have been used to place limits on the radial component of peculiar velocity for A2163 of $v_r = +490_{-880}^{+1370}$ kms $^{-1}$ at 68% confidence. The combination of 142 and 217 GHz observations of A1689 have been used to determine $v_r = +170_{-630}^{+815}$ kms $^{-1}$ (Holzapfel *et al.* 1997b).

6.3. Primary Anisotropies and Source Counts

Although specifically designed to observe the S-Z effect in X-ray selected clusters, the SuZIE receiver is a powerful tool for measuring other anisotropies of the CMB.

In April 1994 we observed, at 142 GHz, two patches of sky, each approximately $36' \times 4'$ and free of known sources. In the ~ 14 hours spent on both patches we reached a flux limit of ≈ 10 mJy for 80 $1.7'$ FWHM pixels. Assuming a Gaussian autocorrelation function for the CMB fluctuations, Church *et al.* (1996) set a 95% confidence upper limit of $\Delta T/T \leq 2.1 \times 10^{-5}$ for a coherence angle of $1.1'$. This result is comparable to limits set by other arcminute scale anisotropy experiments, but is less prone to confusion by radio sources. We anticipate significant increases in both the sensitivity and sky coverage in the near future.

The SuZIE instrument has also been used to investigate structure detected by degree scale CMB anisotropy experiments. During the April 1994 observing run, we scanned two $1^\circ \times 1^\circ$ fields searching for unresolved sources that may be contributing to struc-

ture in degree scale anisotropy measurements (Cheng *et al.* 1994; Gundersen *et al.* 1993). These surveys were performed by slewing the telescope in azimuth at $1'/\text{s}$. The observation of each field took ~ 1.5 hours. Depending on the atmospheric noise in these low-elevation angle ($\sim 20^\circ$) observations, 3σ limits between 0.5 and 1.0 Jy on the brightness of sources less than $2'$ in extent were achieved over the whole field (Church *et al.* 1995).

The surveying capabilities of the SuZIE instrument make it ideal for searching for the S-Z effect in distant clusters. In a low density universe, clusters cease to grow after a redshift $z \sim (\Omega_0^{-1} - 1)^{-1}$. Therefore, information about the number density of S-Z bright clusters at high redshift is a powerful probe of Ω_0 . Unlike the X-ray emission from clusters which is dominated by the emission from the central core radius, the S-Z effect depends only on the quantity of hot gas, not on details of its distribution. In ~ 200 hours of observation, SuZIE could be used to image a $1^\circ \times 1^\circ$ patch of sky to a flux limit of 10 mJy. At this sensitivity, between 3 ($\Omega_0 = 1.0$) and 10 ($\Omega_0 = 0.3$) clusters should be detected (Markevitch *et al.* 1994; Barbosa *et al.* 1996; Eke *et al.* 1996).

7. Conclusion

The SuZIE effort has shown that sensitive millimeter wave observations of the S-Z effect in distant galaxy clusters can be made using ground-based telescopes. Using new filter, detector, and readout technologies the receiver described here produces measurements of differential surface brightness stable on long time scales. Observing with drift scans, which minimize systematic errors, this instrument can be used to measure low surface brightness signals. The sensitivity of the system is limited by residual differential atmospheric emission in all three frequency

bands.

A second, more sensitive, array receiver is under construction. The new receiver will contain an array of four color photometers, each photometer similar in design to that developed for the Far InfraRed Photometer on the InfraRed Telescope in Space (Lange *et al.* 1994). Simultaneous observations will be made at 142, 217, 268, and 360 GHz in each pixel of the array. Multifrequency observations will increase the efficiency of our observations, but more importantly will provide a powerful tool for the removal of residual atmospheric noise. The residual atmospheric noise evident in Fig. 10 can be removed during data reduction by exploiting the difference in the spectra between the atmosphere and the components of the S-Z effect. The removal of atmospheric noise will particularly impact the higher frequency channels and improve the sensitivity to peculiar velocity. With this improvement, the detection of individual cluster peculiar velocities should be possible.

We would like to thank Sabrina Grannan, Teresa Ho, and Ken Ganga for their contributions to observations and data analysis. Thanks to Antony Schinkel and the entire staff of the CSO for their excellent support during the observations. The CSO is operated by the California Institute of Technology under funding from the National Science Foundation, contract #AST-93-13929. This work has been supported by a NSF PYI grant to A. E. Lange, a grant from the David and Lucile Packard foundation and by National Science Foundation grant #AST-95-03226.

REFERENCES

- Afsar, M. N., IEEE Transactions on Instrumentation and Measurement, IM-36, 530
- Alsop, D. C., Inman, C., Lange, A. E., & Wilbanks, T. 1992, Applied Optics, 31, 6610
- Bahcall, N., A., Gramann, M., Cen, R. 1994, ApJ, 436, 23
- Barbosa, D., Bartlett, J., Blanchard, A., & Oukbir, J. 1996, A&A, 262, L21
- Birkinshaw, M., Hughes, J. P., & Arnaud, K. A. 1991, ApJ, 379, 466
- Bock, J. J., & Lange, A. E. 1995, Applied Optics, 34, 7254
- Carlstrom, J.E., Joy, M., & Grego, L. 1996, ApJ, 456, L75
- Cavaliere, A., Danese, L., & DeZotti, G. 1979, A&A, 75, 322
- Chase, S. T., Joseph, R. D., Robertson, N. A., & Ade, P. A. R. 1987, MNRAS, 225, 171
- Cheng, E. S. *et al.* 1994, ApJ, 422, 37
- Church, S. E., Holzapfel, W. L., Ade, P. A. R., Mauskopf, P. D., Wilbanks, T. M., & Lange A. E. 1995, ApJ, 440, 33
- Church, S. E., Ganga, K. M., Holzapfel, W. L., Ade, P. A. R., Mauskopf, P. D., Wilbanks, T. M., & Lange, A. E. 1996, ApJ, in press
- Devlin, M., Lange, A. E., Wilbanks, T., & Sato, S. 1991, IEEE Transactions on Nuclear Science, 40, 162
- Duband, L., Lange, A., & Ravex, A. 1991, Proceedings of the 4th European Symposium on Space Environmental and Control Systems, held in Florence Italy, 21-24 October, 1991 (ESA SP-324, December 1991)
- Ebeling, H., Vogues, W., Bohringer, H., Edge, A. C., Huchra, J. P., & Briel, U. G. 1996, MNRAS, 281, 799
- Eke, V. R., Cole, S., & Frenk, C. S. 1996, MNRAS, 282, 263
- Fischer, M. L. & Lange, A. E. 1993, ApJ, 419, 194
- Glezer, E. N., Lange, A. E., & Wilbanks, T. M. 1992, Applied Optics, 31, 7214
- Gramann, M., Bahcall, N., A., Cen, R., & Gott, R. 1995, ApJ, 441, 449
- Griffin, M. J. & Orton, G. S. 1993, Icarus, 105, 537.
- Gundersen, J. O. *et al.* 1993, ApJ, 413, L1
- Haller, E. E. 1985, Infrared Physics, 25, 257
- Halpern, M., Gush, H. P., Wishnow, E., & De Cosmo, V. 1986, Applied Optics, 25, 565
- Herbig, T., Lawrence, C. R., Readhead, A. C. S. & Gulkis, S. 1995, ApJ, 449, L5

- Holzzapfel, W. L., Arnaud, M., Ade, P. A. R., Church, S. E., Fischer, M. L., Maukopf, P. D., Rephaeli, Y., Wilbanks, T. M., & Lange A. E. 1996a, ApJ, in press
- Holzzapfel, W. L., Ade, P. A. R., Church, S. E., Maukopf, P. D., Rephaeli, Y., Wilbanks, T. M., & Lange A. E. 1996b, ApJ, in press
- Jones, M. *et al.* 1993, Nature, 365, 320
- Kudō, K. 1972, Kiso Bussei Zuhyō: Bunkōgakuteki Seishitsu o Shu to Shita (Tokyo: Kyōritsu Shuppan)
- Lange, A. E., Freund, M. M., Sato, S., Hirao, T., Matsumoto, T., & Watabe, T. 1994, ApJ, 428, 384
- Lis, D. C., Serabyn, G. 1996 Private Communication
- Markevitch, M., Blumenthal, G. R., Forman, W., Jones, C., & Sunyaev, R. 1994, ApJ, 426, 1
- Meyer, S. S., Jeffries, A. D., & Weiss, R. 1983, ApJ, 271, L1
- Myers, S. T., Baker, J. E., Readhead, A. C. S., & Herbig, T. 1995, ApJ, submitted
- Orton, G. S., Griffin, M. J., Ade, P. A. R., Nolt, I. G., Radostitz, J. V., Robson, E. I., & Gear, W. K. 1986, Icarus, 67, 289
- Radford, S. J. E., Boynton, P. E., Ulich, B. L., Partridge, R. B., Schommer, R. A., Stark, A. A., Wilson, R. W., & Murray, S. S. 1986, ApJ, 300, 159
- Rephaeli, Y., & Lahav, O. 1991, ApJ, 372, 21
- Rephaeli, Y. 1994, ApJ, 445, 33
- Rieke, F. M., Lange, A. E., Beeman, J. W., & Haller, E. E. 1989, IEEE Transactions on Nuclear Science, 36, 946
- Sunyaev, R. A., & Zel'dovich, Ya. B. 1972, Comments on Astrophysics and Space Physics, 4, 173
- Uson, J. 1987, NRAO Green Bank Workshop 16, O'Dea, C., & Uson J., Green Bank, WV.: NRAO, 255
- Wilbanks, T., Devlin, M., Lange, A. E., Sato, S., Beeman, J. W., & Haller, E. E. 1990, IEEE Transactions on Nuclear Science, 37, 566
- Wilbanks, T. M., Ade, P. A. R., Fischer, M. L., Holzzapfel, W. L., & Lange, A. E. 1994, ApJ, 427, L75
- Zel'dovich, Ya. B. & Sunyaev, R. A. 1968, Astrophysics and Space Sciences, 4, 301